Flow Turbulence Combust (2013) 91:565–585
DOI 10.1007/s10494-013-9489-1

Coherent Structures in Oscillating Turbulent Boundary Layers Over a Fixed Rippled Bed

D. G. E. Grigoriadis · E. Balaras · A. A. Dimas

Received: 29 October 2012 / Accepted: 8 July 2013 / Published online: 31 July 2013

Abstract Coherent structures generated by oscillating turbulent boundary layers with or without a unidirectional current over a fixed, rippled bed are presented. The effect of ripple height and current intensity on the characteristics of these structures was investigated using a series of large-eddy simulations performed at $Re_\alpha = 23{,}163$. These flows are typical in coastal regions where complex wave-current interactions occur. A cartesian flow solver was used with the rippled bed represented using the immersed boundary (IMB) method. Results are presented for three ripple steepness values and two current magnitudes. Three different types of coherent structures were identified with their size, shape and evolution largely depending on ripple steepness, while, their potential effect on sediment transport is discussed.

Keywords LES · Oscillatory boundary layer · Coherent structures · Finite difference methods · Immersed boundary method

Electronic supplementary material The online version of this article (doi:10.1007/s10494-013-9489-1) contains supplementary material, which is available to authorized users.

D. G. E. Grigoriadis (✉)
Computational Sciences laboratory UCY-CompSci, NIREAS water center,
Department of Mechanical and Manufacturing Engineering,
University of Cyprus, Nicosia, Cyprus
e-mail: grigoria@ucy.ac.cy

E. Balaras
Department of Mechanical and Aerospace Engineering,
The George Washington University, Washington, DC 20052, USA
e-mail: balaras@email.gwu.edu

A. A. Dimas
Department of Civil Engineering,
University of Patras, Patras 26500, Greece
e-mail: adimas@upatras.gr

1 Introduction

The wave-induced flow over a rippled bed is of particular interest in coastal engineering applications, i.e., sediment transport. In general, the flow consists of an oscillatory component due to wave propagation and a unidirectional one due to wave-generated or other current. A model of this wave-current flow, far above the bed, is the following combined oscillatory-unidirectional external flow

$$u_o = U_C + U_o \sin(\omega t) \tag{1}$$

where U_C is the current velocity, U_o is the wave velocity and U_C/U_o represents the relative strength of the current. The radial frequency of oscillation is $\omega = 2\pi/T$ where T is the wave period. The characteristic length scale of the external flow is the amplitude of the orbital motion, $\alpha_o = U_o/\omega$. The relevant dynamic dimensionless groups are the Reynolds and Keulegan–Carpenter numbers,

$$Re_\alpha = \frac{U_o \alpha_o}{\nu} = \frac{{U_o}^2}{\omega \nu} \quad \text{and} \quad KC_h = \frac{U_o}{\omega h_r} = \frac{\alpha_o}{h_r} \tag{2}$$

where the Keulegan–Carpenter number KC_h, is defined with respect to the ripple height h_r for each case (see Table 1). The characteristic geometrical dimensions of coastal bed ripples are their length, L_r, and height, h_r. In general, sand ripples are classified as orbital, suborbital or anorbital [21, 22, 30]. The orbital ripples are the steepest ($h_r/L_r > 0.1$) and their length is proportional to and on the order of the diameter of the orbital motion. The anorbital ripples appear when the diameter of the orbital motion is large relative to the sand particle size, which results into ripples with very mild steepness and short length ($L_r/\alpha_o) < 0.1$). The dimensions of suborbital ripples lie between those of orbital and anorbital. Orbital and the larger suborbital ripples are also called vortex ripples because a vortex is formed due to separation at their crests twice every wave period. A typical vortex ripple is shown in Fig. 1. Here, the ripple trough is assumed to have a circular-arc shape of radius r_r, leading to ripples with sharp crests. Typical ripple dimensions, according to field and experimental data [10, 21], are

$$\frac{L_r}{\alpha_o} \lessapprox 2.2 \quad \text{and} \quad \frac{h_r}{L_r} \lessapprox 0.2 \tag{3}$$

So far, the oscillatory boundary layer over a flat bed has been investigated by several researchers both experimentally [15, 18] and numerically [25, 26]. In comparison to a flat bed, the existence of ripples significantly modifies the flow

Table 1 Summary of computational cases at $Re_\alpha = 23{,}163$

Case	U_C/U_o	h_r/L_r	KC_h
A0	–	0.125	3.636
B0	–	0.159	2.859
C0	–	0.200	2.272
B1	0.5	0.159	2.859
B2	1.0	0.159	2.859

A0–C0: purely oscillatory flow cases. B1–B2: oscillatory-unidirectional flow cases

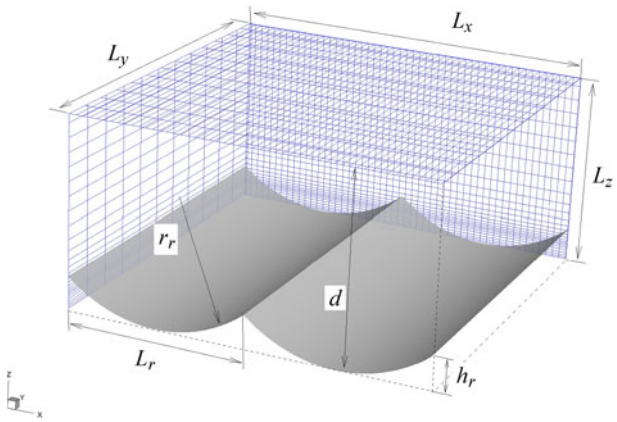

Fig. 1 Computational domain and typical grid resolution (only every 10th computational node is shown) for the oscillatory flow over rippled bed at $Re_\alpha = 23{,}163$

dynamics in the near wall region, mainly due to flow separation and vortex shedding at the ripple crest. In these cases, the appearance of stronger secondary turbulent motions such as those produced by coherent structures, affect the spatiotemporal distribution of the wall shear stress. These effects are of particular interest in coastal applications and they are expected to have a profound impact on the sediment incipient motion, bed load and suspended sediment transport [23, 24, 33].

The unidirectional, steady flow over ripples has been studied using Direct Numerical Simulations (DNS) [20], and later using large-eddy simulations (LES) [6, 7, 14]. For the oscillatory flow, Scandura et al. [27] presented DNS results for smooth-crested ripples at relatively low Reynolds numbers ($Re_\alpha = 1{,}005$) at the onset of transition, and Barr et al. [3] performed coarse DNS calculations also over smooth-crested ripples at $Re_\alpha = 15{,}600$. Chou and Fringer [7] presented coupled LES over an erodible bed to study the dynamic formation and evolution of ripples. To reduce the computational cost, in most oscillatory flow cases, the Reynolds-averaged Navier–Stokes (RANS) equations are solved. Fredsøe et al. [11], for example, presented a combined experimental/numerical study of the flow over a rippled bed using laser Doppler anemometry (LDA) to measure velocity statistics over the ripples. In the numerical part of this study [11], a $k-\omega$ turbulence model [31] was used, which is usually more accurate than the standard $k-\epsilon$ model in separated flows. The overall agreement between the experiments and the computations was satisfactory but comparisons were limited to the streamwise horizontal component of velocity.

Recently, we have presented LES of the turbulent boundary layer over vortex ripples, at $Re_\alpha = 23, 163$, using the external flow given by Eq. 1, and examined in detail the effect of ripple height and current strength on the mean flow and turbulence statistics [12]. It was found that all results are influenced mainly by the oscillatory nature of the flow and the ripple height. The effect of current strength was found to be relatively weak on the forces and the flow patterns developed over the ripples.

The motion of suspended sediment has also been studied both for unidirectional [8, 32] and oscillatory flows [24, 33]. In all of these studies, the importance of instantaneous, coherent flow features on bed shear stress and suspended sediment transport patterns is demonstrated.

In the present study, our primary objective is to extend the work in [12] by reporting and analysing the formation, shape and evolution of turbulent coherent structures

as a function of ripple height and current strength. Here, we focus on instantaneous flow features: we identify and track the evolution of coherent structures, and discuss how these could affect sediment transport. All computational cases reported here were produced using a structured Cartesian solver with optimal conservation properties combined with the immersed boundary (IMB) method, which facilitates the incorporation of complex bed shapes in a cost/efficient manner (see details in [12]).

In the following Section 2, we summarise the mathematical formulation and the numerical method including the procedure to generate the oscillatory motion over the bed. The parametrization (flow and computational) is presented in Section 3, while results are presented and discussed in Section 4.

2 Formulation and Numerical Method

In the LES approach, all flow structures are separated into the large, energy-containing eddies, which are directly resolved by the computational grid as in the DNS approach, and the sub-grid contribution (SGS), which are parametrized. Using the characteristic length scales of α_o, U_o and $\frac{1}{2}\rho {U_o}^2$, velocity and pressure, the resulting non-dimensional equations of motion for an incompressible flow become,

$$\frac{\partial \overline{u}_i}{\partial x_i} = 0 \tag{4}$$

$$\frac{\partial \overline{u}_i}{\partial t} + \frac{\partial \overline{u}_i \overline{u}_j}{\partial x_j} = -\frac{\partial p}{\partial x_i} - \frac{\partial \tau_{ij}}{\partial x_j} + \frac{1}{Re_\alpha}\frac{\partial {\overline{u}_i}^2}{\partial x_j \partial x_j} + f_i \tag{5}$$

where x_i ($i = 1, 2, 3$) are the three Cartesian coordinates (denoted x, y, z, hereafter), $\overline{u}_i$ are the resolved velocity components in the corresponding directions (denoted u, v, w, hereafter), p is the pressure, $\tau_{ij} = \overline{u_i u_j} - \overline{u}_i \overline{u}_j$ are the SGS stresses and Re is the Reynolds number defined in the previous section. The source term f_i is an external forcing function, associated with the immersed boundary method, to mimic the existence of the ripple boundary. To parameterize the SGS stresses, τ_{ij}, an eddy-viscosity type model is used:

$$\tau_{ij} = -2\nu_T S_{ij} \tag{6}$$

where ν_T is the eddy-viscosity and $S_{ij} = (1/2)(\partial \overline{u}_i/\partial x_j + \partial \overline{u}_j/\partial x_i)$ is the resolved strain rate tensor. The eddy viscosity is computed using the Filtered Structure Function (FSF) model developed by [9]:

$$\nu_T(x,t) = 0.0014 C_K^{-3/2} \overline{\Delta} \left(\overline{F_2}\left(x, \overline{\Delta}, t\right)\right)^{1/2} \tag{7}$$

where $C_K = 1.4$ is the Kolmogorov constant, $\overline{\Delta} = (\Delta x \Delta y \Delta z)^{1/3}$ is the filter width, and $\overline{F_2}$ is a filtered, second order, structure function. Details on the FSF model formulation can be found in [9]. A detailed validation of the present implementation can be found in [13] for the unidirectional flow over dunes and in [12] for the oscillating flow over ripples.

The Cartesian flow solver using Eqs. 4 and 5 which govern the evolution of the larger, resolved scales, is based on a fully explicit fractional step, projection method.

Space discretisation is using a central, second order finite-differences scheme on a staggered variable arrangement. Time advancement is performed using a fully explicit Adams–Bashforth scheme (see [13] for details).

In order to enforce the no-slip condition along the ripple's surface, an immersed boundary method is used. At this part of the computational domain, the solution is locally reconstructed in the vicinity of the boundaries, since the bed surface is not aligned with the grid lines. The main advantage of this approach is that the efficient, energy conserving Cartesian solvers, which have been routinely used in DNS and LES over the past years, can be applied to complex geometrical configurations in a straightforward manner. In our implementation, the rippled bed is identified by a series of material-fixed interfacial markers whose location is defined in the reference configuration of the solid. This information is then used to identify the Eulerian grid nodes involved in the reconstruction of the solution near the boundary in a way that the desired boundary conditions for the fluid are satisfied. The reconstruction is performed 'around' the points in the fluid phase closest to the solid boundary (all points that have least one neighbor in the solid phase). The details of the tracking scheme and the solution reconstruction, for stationary boundaries, can be found in [2]. The resulting solver has excellent parallel efficiency, requires 120 Mb of physical memory per million nodes, and requires less than 0.07s/iteration per million nodes, on low-cost personal computers (e.g. a single socket PC using a six-core CPU such as an AMD-Phenom processor at 3.2GHz).

The key element of performing the simulations presented below is the generation of the external velocity field given by Eq. 1. We decompose the external far-field velocity variation into a steady (current) component U_C, and a zero-mean oscillatory component. The requested variation of the external field is achieved by imposing an appropriate pressure gradient variation for each case. For this purpose, a time-varying pressure gradient is introduced into the streamwise momentum equation:

$$\frac{dp}{dx} = \left(\frac{\Delta P}{\Delta x}\right)_C + \omega U_o \left(\cos\left(\omega t\right)\right) \tag{8}$$

The first term in the RHS of Eq. 8 acts as a body force which generates a current of bulk velocity U_C. This term is only active in cases where a unidirectional current exists (cases B1 and B2 with $U_C/U_o \neq 0$ in Table 1). To evaluate this steady-current component of the external flow, a preliminary unidirectional simulation was first conducted to obtain the mean pressure gradient component $(\Delta P/\Delta x)_C$ of Eq. 8, which results at the required bulk current velocity U_C. The last term in Eq. 8 generates a purely sinusoidal zero-mean external oscillatory flow with a velocity amplitude U_o. This forcing term was computed during the simulation for all cases reported here (Table 1).

3 Computational Setup and Parametric Space

Table 1 summarizes the cases we considered in the present work at Reynolds number, $Re_\alpha = 23, 163$. Computations were conducted for three different ripple heights, $h_r/L_r = 0.125, 0.159, 0.20$, and two different current strengths, $U_C/U_o = 0.5, 1.0$. Using these parameters, cases without a unidirectional current correspond to the

wave dominated regime while cases with a current to a *current dominated regime* according to [28]. For all cases the bed consists of two-dimensional, rigid ripples with sharp crests to match the experimental conditions in [11]. In actual sand ripples, the sharp crests will be rounded under the action of shear stress [7], and the ripple shape will eventually become three-dimensional and asymmetric due to sediment transport. Such effects are not accounted for in our computations, where a fixed, hydraulically smooth bed surface configuration is assumed. This means that our results are applicable to a sandy bed surface, as long as the corresponding grain diameter, D_s, is smaller than half the thickness of the viscous sublayer:

$$\frac{D_s u^*_{\max}}{\nu} = \frac{D_s}{\alpha_o}\frac{u^*_{\max}}{U_o} Re_\alpha \leq \frac{11.6}{2} \tag{9}$$

where $u^*_{\max}$ is the maximum friction velocity during a wave period, and 11.6 is the thickness of the viscous sublayer in wall coordinates according to [10]. For $h_r/L_r = 0.159$, $\alpha_o = 9.6$cm and $T = 2.5$s, which correspond to the experimental case in [11], we found in [12] that $u^*_{\max}/U_o \approx 0.1$, therefore, from Eq. 9, we get $D_s \leq 0.24$ mm. The corresponding mobility number is:

$$\Psi = \frac{(\alpha_o \omega)^2}{(S-1)\, g D_s} \geq 15 \tag{10}$$

where $S = 2.65$ is the specific gravity of sand. For $\Psi = 15$, the ripple steepness $h_r/L_r = 0.159$ of case B0 (see Table 1) is within the observed values reported in [21]. Using B0 as the base case, we will examine the effect of ripple steepness (cases A0, B0 and C0) and current strength (cases B1 and B2). Note that the ripple steepness of cases A0, B0 and C0 are also, in general, within the observed values reported in [21].

The computational domain used for the present simulations has dimensions of $L_x = 2L_r$, $L_y = 2L_r$, and $L_z = 0.954L_r$ (see Fig. 1). Two ripples were included along the streamwise direction with a length $L_r = 2.2\alpha_o$. The spanwise length of the computational box was determined using preliminary simulations ensuring that values of two-point correlations remain small in order to contain the largest structures that are important to the flow dynamics. The size of the domain along the vertical direction was set to $L_z = 4.2\alpha_o$ to match the experimental conditions in [11]. Periodic boundary conditions are used both in the streamwise and spanwise directions. The immersed boundary method was used to impose the no-slip boundary condition on the solid rippled bed. Along the top boundary, a slip boundary condition was used.

The computational grid is identical to the one used in [12], consisting of $512 \times 128 \times 256$ nodes in the streamwise, spanwise and vertical directions, respectively. It is uniform in the streamwise and spanwise directions and stretched in the vertical direction to cluster points near the rippled bed. The numerical resolution along the three directions is: $\Delta x/\alpha_o = 9 \times 10^{-3}$, $\Delta y/\alpha_o = 3.6 \times 10^{-2}$ and $3.6 \times 10^{-3} < \Delta z/\alpha_o < 3.1 \times 10^{-2}$. Approximately 72 nodes are used to resolve a vertical length equal to the ripple height above the bed. The corresponding grid spacing in wall units during the cycle lead to maximum values of $\Delta s^+ \simeq 8.8$ parallel to the bed, $\Delta y^+ \simeq 30$ along the spanwise direction and $\Delta n^+ \simeq 1.9$ in the wall-normal direction, which was found sufficient to resolve the near wall structures as well as the outer flow as explained in [12].

A detailed validation of our computations for cases with a unidirectional current only and the oscillatory flow with and without a current together with a grid refinement study is presented in [12] and will not be discussed here. Overall the computed mean velocity field as well as the velocity fluctuations were found in good agreement with the experimental results reported in [11].

4 Results

4.1 Overview

The focus of the present work is on the dynamics of the coherent structures appearing in such flows and how they are affected dy the ripple height and current strength. For this purpose, in each flow case we utilized a data-set consisting of 720 instantaneous snapshots, covering six to ten cycles of oscillations. The coherent structures were identified using different methods such as: (i) locating vortex cores which correspond to low pressure fluctuations p', (ii) using the second invariant of the velocity gradient tensor, Q, (see [17]) or (iii) using the λ_2 criterion (see [19]). Figure 2 compares the p' and λ_2 criterion for the identification of coherent structures in a typical instantaneous snapshot. Both methods reveal similar structures at least for the most organised ones. In the following, we will mostly present structures identified by p', but in all cases results where cross-checked with the other criteria for consistency.

To better quantify the effect of coherent structures on sediment transport, we also used a quadrant analysis (see [29]), where four types of events are identified as shown in Fig. 3a. Of particular interest are *ejection* and *sweep* events, which can be directly correlated to the deposition or uplifting of sediment from the bed. We should note that due to the flow reversal during the decelerating phase of the cycle ($180° < \omega t < 360°$), *sweeps* and *ejections* have to be reclassified into a different quadrant as shown in Fig. 3b.

Due to the existence of strong adverse/favourable pressure gradients, the structures forming over the rippled bed resemble those found on flat plate boundary-layers, only during parts of the cycle. From all cases we have examined, coherent structures had a high degree of intermittency and were rapidly changing characteristics during the cycle. Overall, three commonly dominant structures were identified for different parts of the cycle: (i) spanwise rollers forming at the lee side of the ripple, (ii) lambda structures and (iii) arch-like vortices. In the following paragraphs we discuss their evolution and dynamics, and how they are affected by the ripple steepness and the relative current strength.

4.2 Coherent structure dynamics

The spanwise rollers form just downstream of the ripple crest along the lee side during the early acceleration phase ($\omega t \lesssim 75°$ and $180° \lesssim \omega t \lesssim 255°$) as shown in Figs. 4 and 5. At their early stages, these rollers are nearly two-dimensional. They start as quasi two-dimensional spanwise roller structures, which is the result of instability of the free-shear layer originating at the crests. Due to the sharpness of the ripples considered in the present work (Fig. 1), the separation point is fixed

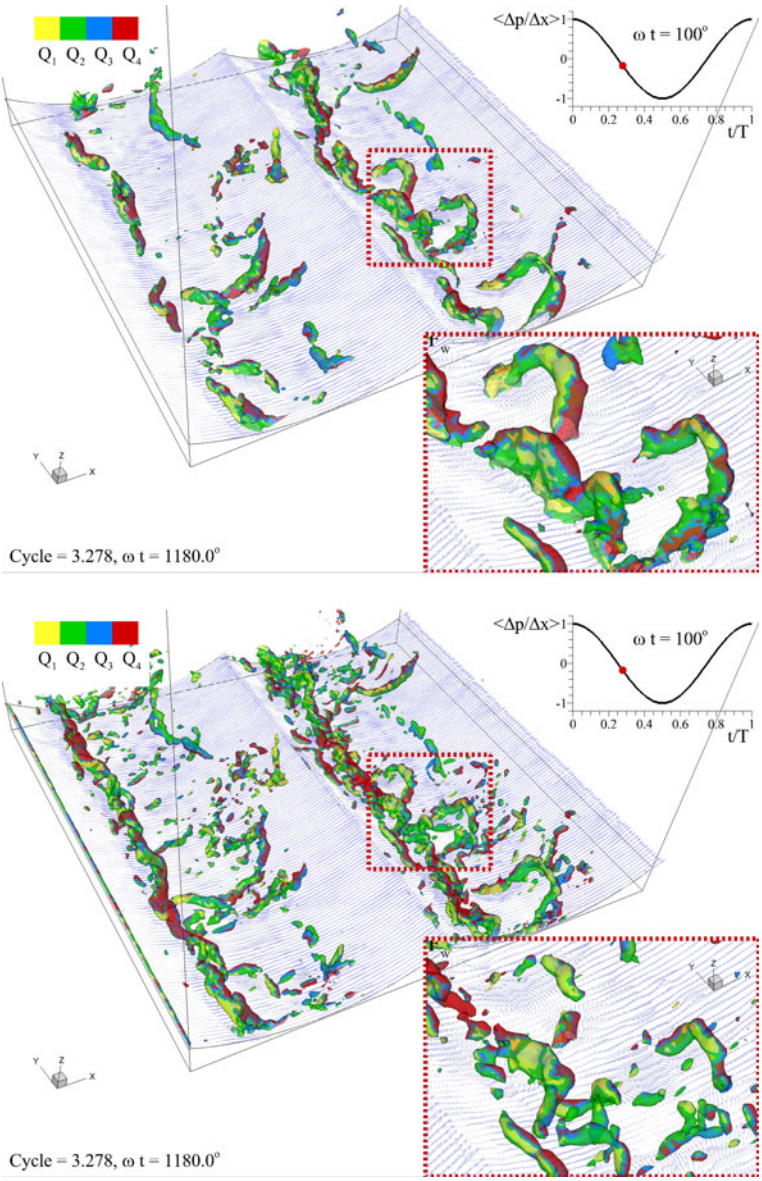

Fig. 2 Different vortex identification methods, (*top*) iso-surfaces of negative pressure fluctuations and (*bottom*) λ_2 criterion of Jeong and Hussain [19]. Case A0 at $\omega t = 100°$. *Colors* correspond to dominant quadrant events and the vector field to the wall shear stress components along the bed

and the boundary layer always detaches at the crests. Consequently, the free-shear layer generated at the crests gradually rolls up to form these quasi two-dimensional spanwise vortices. At later time during the cycle, as these structures are convected downstream they are subjected to lateral instabilities, interact with the wall or other structures, become distorted, and eventually become highly three-dimensional. An

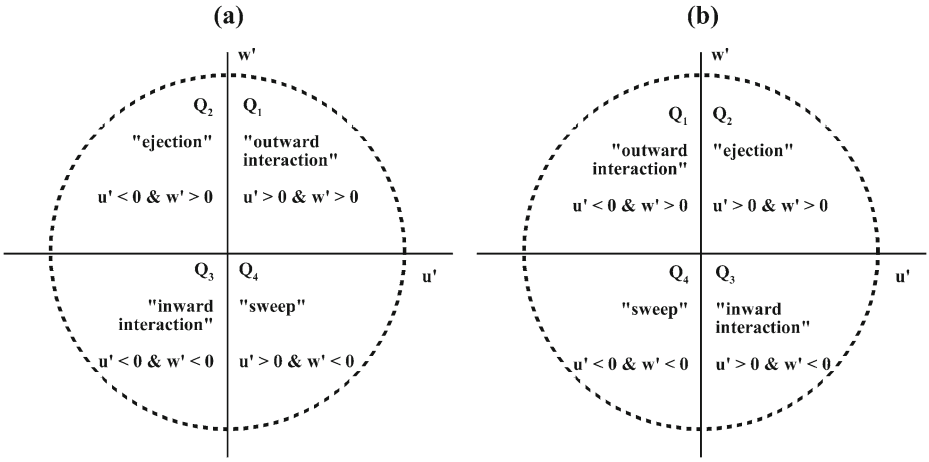

Fig. 3 Definition of the quadrant analysis events for the positive velocity part of the cycle during $0° < \omega t < 180°$ (*left*), and for the part of the cycle when flow reverses direction during $180° < \omega t < 360°$ (*right*)

example is shown in Fig. 4, where one can follow the evolution of these rollers for the three ripple heights, i.e. cases A0, B0 and C0. Depending on their initial strength of rotation, occasionally, large fragments of these rollers could survive even after the deceleration phase as shorter (along the spanwise direction) isolated rollers. In such events, these fragments could even reach the next crest, fly over it and interact with the new primary roller which forms below the shear layer of the next crest.

For the smallest ripple height (case A0) these rollers are initially highly coherent covering almost the full extent of the spanwise domain (Fig. 4a), remaining very close to the near wall region as they move on the downslope. As the ripple height is increased, the interaction of these structures with the wall becomes weaker. In addition, the increased radius of ripple-curvature generates more energetic detached shear layers (see also Fig. 12 in [12]), which roll-up into much stronger spanwise rollers. The higher the ripple height the further away from the bed these rollers are ejected and evolve rapidly into highly three-dimensional structures through vortex interactions and pairings (Fig. 4b and c). As already mentioned in [12], the presence of a unidirectional current does modify the characteristics of the flow primarily during the deceleration phase. As a result, the effect of current strength on the spanwise rollers is mainly noticeable during flow reversal. When the flow accelerates opposite to the current direction, a stronger shear layer forms at the crest, generating larger and more energetic vortical rollers as shown in Fig. 5. We should also note that one of the main factors for the loss of spanwise coherence of the roller structures, particularly for steeper ripples, is their interaction with strong streamwise vortices, which are formed at the late acceleration phases. At the later part of the cycle ($\omega t \gtrsim 75°$ and $\omega t \gtrsim 255°$) and while the flow still accelerates, these interactions lead to a gradual break up and fragmentation of the spanwise rollers.

The second type of structures identified in the flow field are lambda-shaped vortices which resemble those found in non-oscillatory turbulent boundary layers. These were found to form along the ripple troughs as the one shown in Fig. 6 for

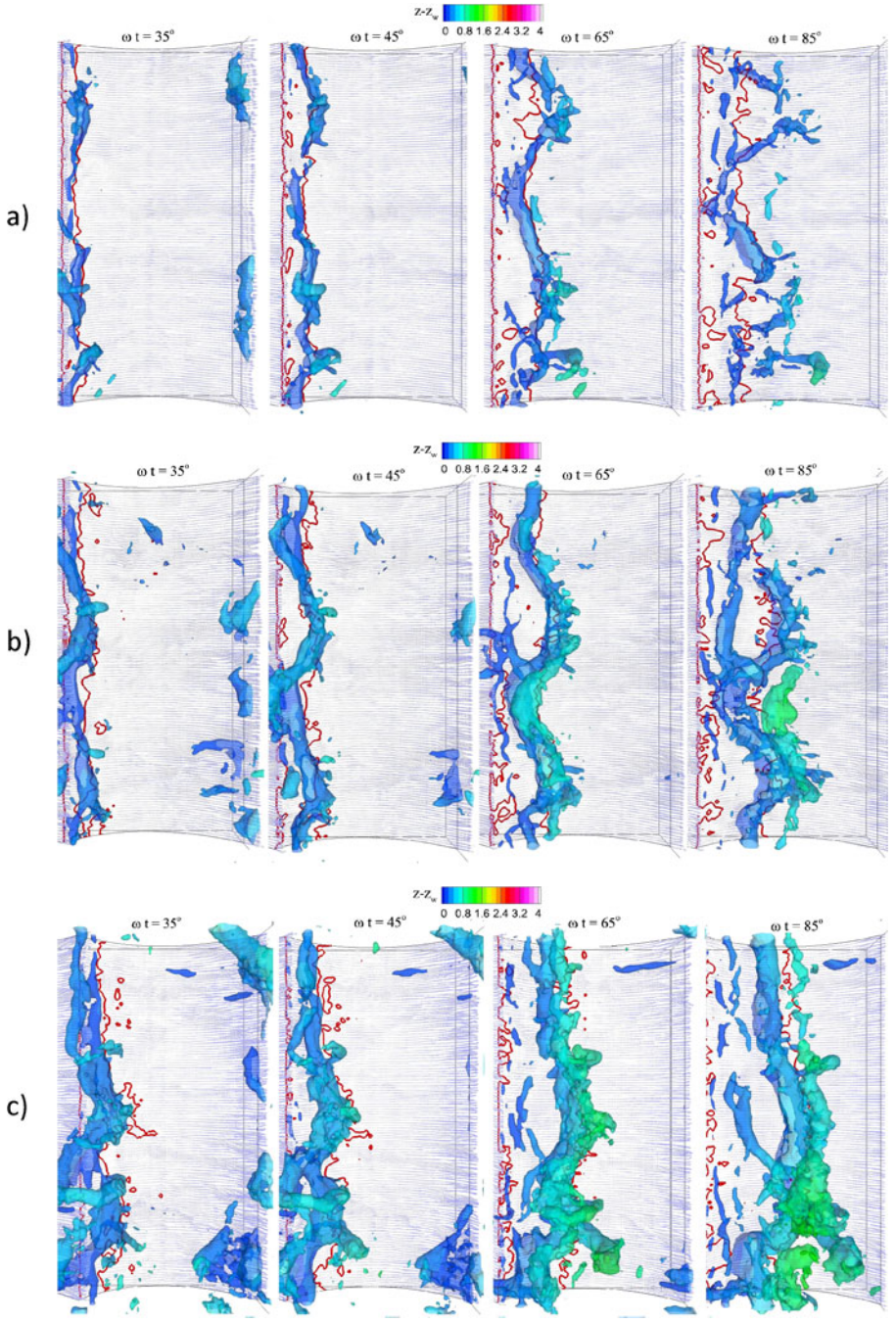

Fig. 4 Spanwise roller structures developing at the early stages of positive external velocity for different ripple heights identified as pressure fluctuations $p'/\left(\frac{1}{2}\rho {U_0}^2\right) = -0.2$. (*top*) case A0, (*middle*) case B0, (*bottom*) case C0. *Colors* correspond to the local distance from the wall and the vector field to the wall shear stress components along the bed. The *red line* is the locus of change of sign for the streamwise component of wall shear stress

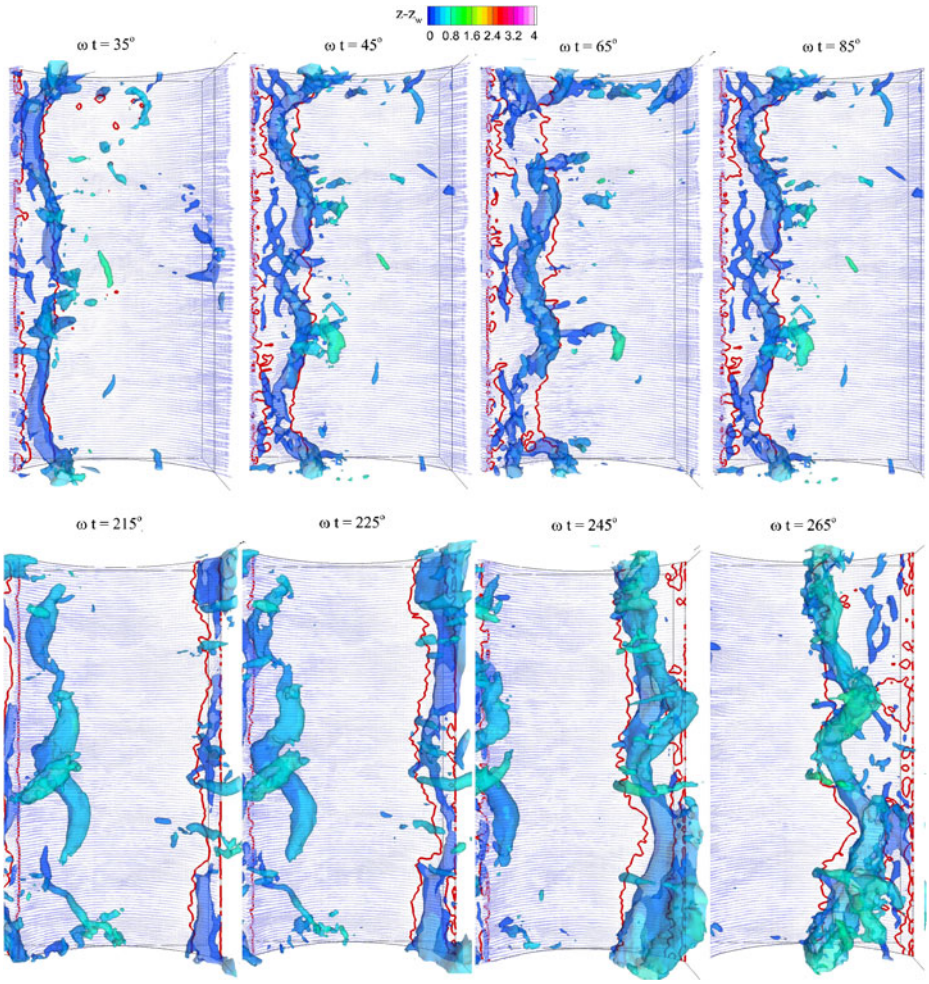

Fig. 5 Effect of a unidirectional current on the typical evolution of spanwise rollers for case B1. The direction of the current is from left to right. (*top figures*) spanwise roller evolution at phases of positive external velocity, (*bottom figures*) spanwise roller forming during phases of flow reversal, opposite to the current. The *red line* is the locus of change of sign for the streamwise component of wall shear stress and the *color* corresponds to the local distance from the wall

Case A0. Similar structures were also recorded for cases with steeper ripples. The size and strength of these structures correlates with that of the spanwise rollers, and therefore it is directly related to the ripple height (see Figs. 6 and 7). In particular, lambda structures were found to be generated indirectly by fragments of the distorted primary rollers which interacted with streamwise vortices becoming warped and stretched around vortex lines [4]. The life-span of these structures was less than a sixth of a period and they typically appeared during $\omega t \approx 60^\circ - 180^\circ$ and $\omega t \approx 240^\circ - 360^\circ$.

We should also mention that especially for the steepest ripples, strong and relatively long streamwise vortices as those shown in Fig. 8 appeared to form along the

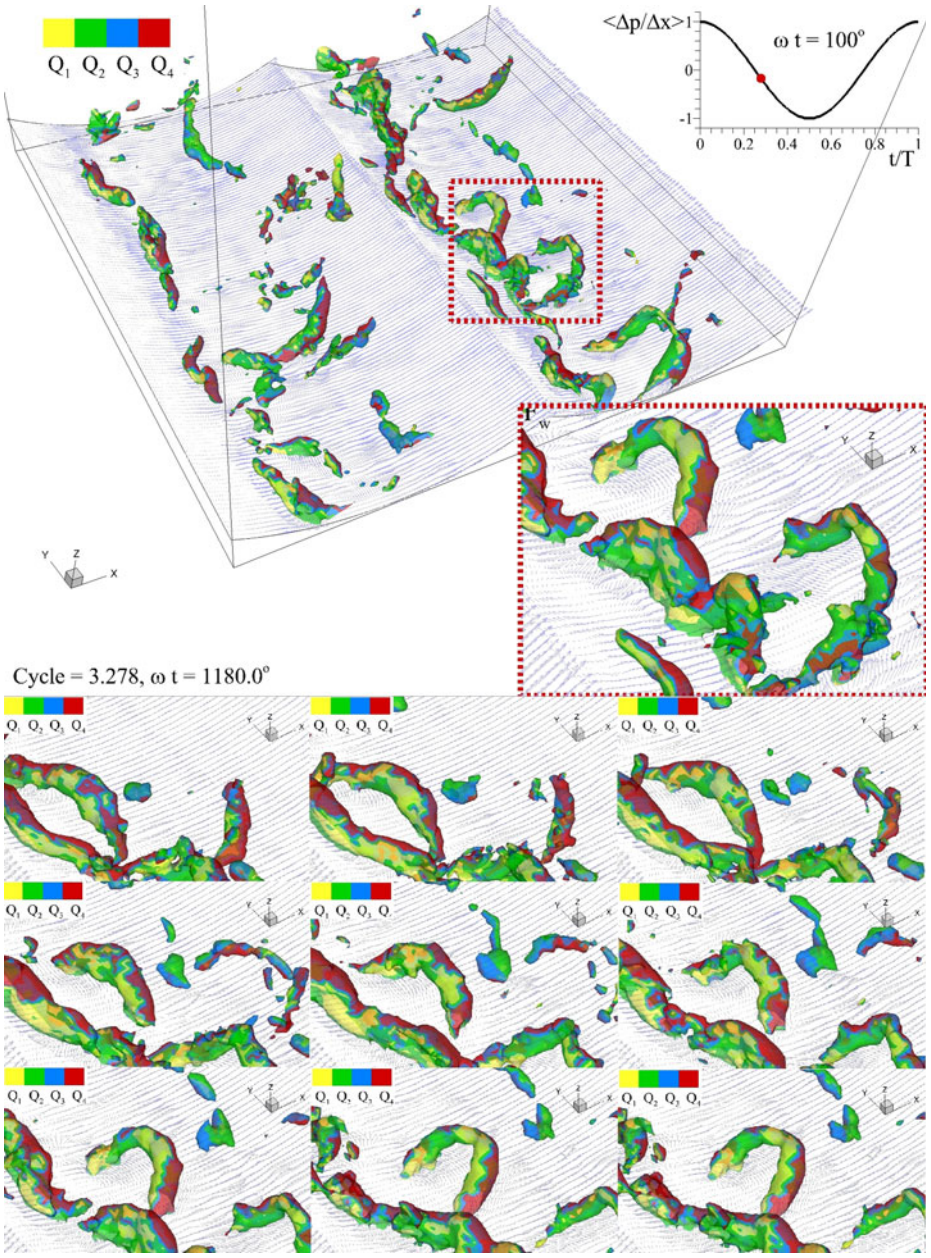

Fig. 6 Instantaneous snapshot of a lambda coherent structure for Case A0 (*top*) and its time evolution (*below*) between 70–110° at intervals of 5°. The *color* corresponds to the local distance from the wall

lee side of the ripple after the primary roller. Although not systematically appearing as vortex pairs, these structures resemble those produced by a Görtler instability which is typical of boundary layers over concave surfaces. Similar structures have

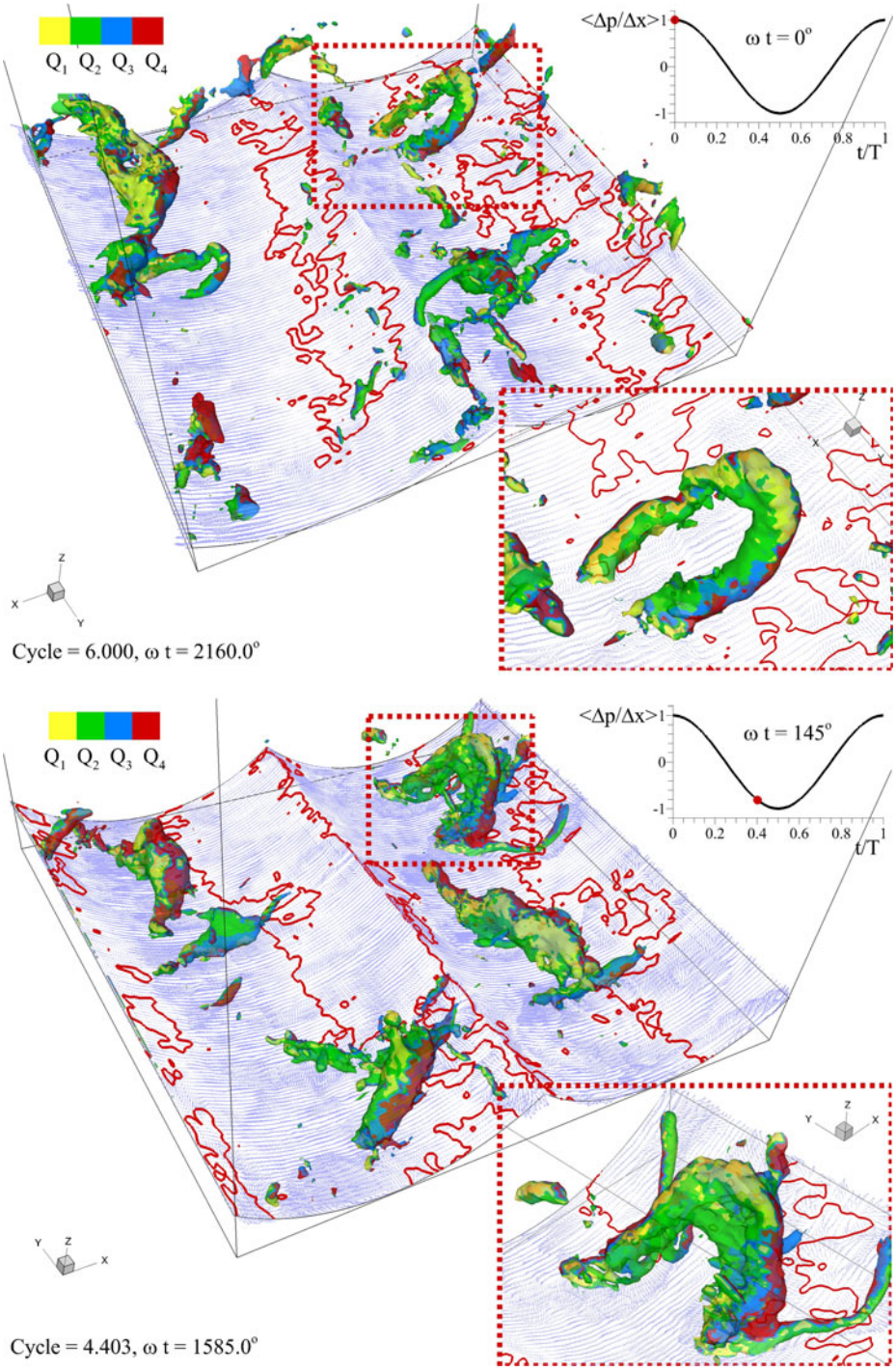

Fig. 7 Instantaneous snapshots of lambda coherent structures for case B0 at $\omega t = 0°$ (*upper figures*), and case C0 at $\omega t = 145°$ (*bottom figures*). The *color* corresponds to the local distance from the wall

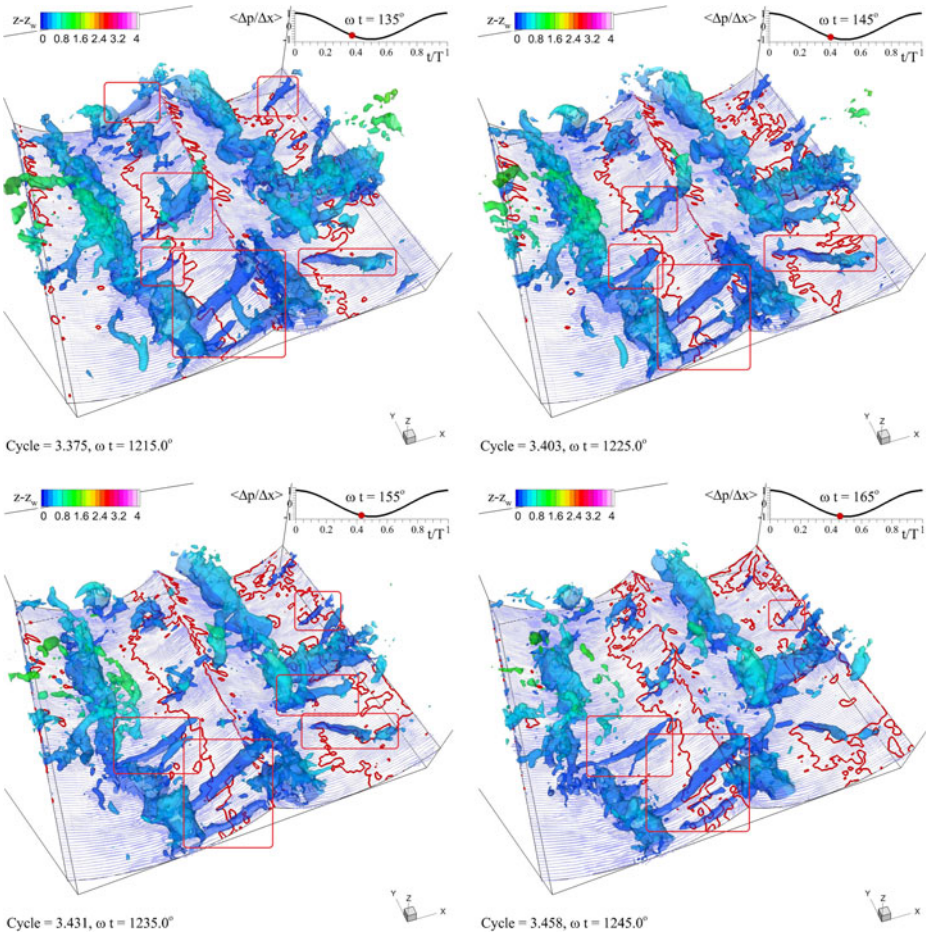

Fig. 8 Evolution of large streamwise vortices for Cases C0 before flow reversal, $\omega t = 135 - 165°$. The *color* corresponds to the local distance from the wall

been observed both computationally and experimentally in the literature for flows over wavy walls [5, 32], playing a crucial role on sediment erosion [1, 16]. To investigate the importance of such an instability to the formation of these vortices, following the definition of Calhoun & Street in [5], the Görtler parameter, $G(\phi) = <U(\phi)> (\kappa(\phi) L_r)^2/(\nu L_r)$, was computed for each case. This number represents the ratio of curvature effects to viscous effects with $\kappa(\phi)$ in the above expression being the local slope of the streamlines. Figure 9 shows the effect of ripple size on the cycle averaged Görtler parameter G. Regions of strong positive values indicate possible areas of generation of Görtler vortices. The spatiotemporal variations of G, correlate with the onset of strong streamwise vortices. As expected, the higher curvature of the streamlines for steeper ripples, makes them more prone to instabilities, which agrees with the stronger streamwise vortices produced in these cases and their interaction with the spanwise rollers, as shown in Fig. 8.

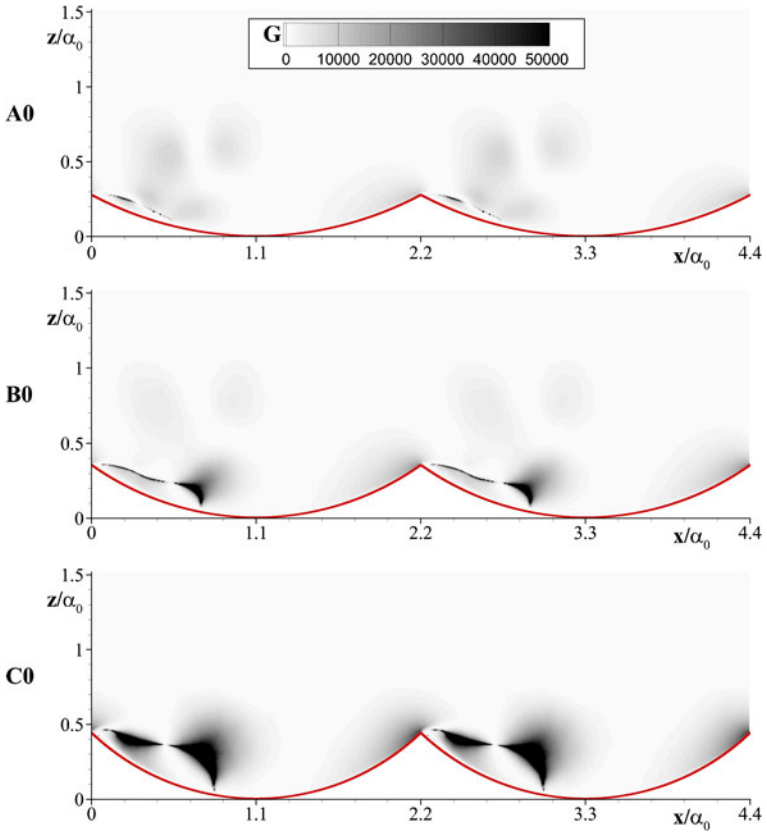

Fig. 9 Effect of ripple height on the cycle averaged Görtler parameter for Cases A0, B0 and C0 at $\omega t = 60°$, i.e., positive external velocity

The last dominant structure that was a common feature of the cases examined, resembles bended, arch-shaped, tornado-like structures such as the one shown in Fig. 10. These were also found to be generated from the rollers but evolved in a completely different manner. In occasions where a spanwise roller interacts with an isolated streamwise vortex, secondary motions are induced along the streamwise direction. At the early stages of acceleration, these secondary motions start to organize as arch-like structures wrapped around the rollers at their downstream side. Even after the fragmentation of the spanwise roller, these structures continue to exist as they travel downstream.

Interestingly enough, these "arches" form in planes vertical to the spanwise direction with their "legs" pointing upwind. Their size and life-span were also found to strongly depend on the ripple height, with steeper ripples generating more energetic and larger arch-like structures. In several cases, their extend was found to be as large as $L_r/2$ for the steeper ripples. In the presence of a unidirectional current, these structures were captured for both the forward and the backwards parts of the cycle. At the late stages of acceleration ($\omega t \gtrsim 75°$ and $\omega t \gtrsim 255°$), the upper leg of these structures travels faster and eventually detaches completely from the recirculation

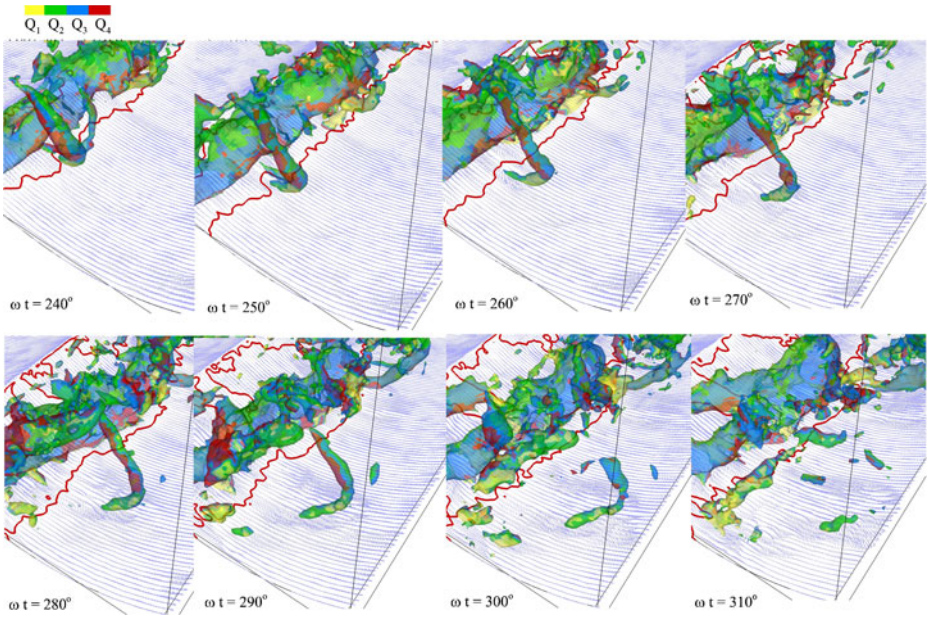

Fig. 10 Typical evolution of an arch-like structure for case B0 during $\omega t = 240 - 310°$. The *color* corresponds to the local quadrant event

region as it is advected by the outer flow. The shear action of the outer flow elongates them further until they are either dissolved or collapse along the bed before the next crest.

4.3 Effect of coherent structures on bed stress

For all cases examined, it is also evident that the characteristics and evolution of the structures described in the previous section, strongly affect the distribution of bed shear stress. It is therefore expected that they play a crucial role on sediment motions. Rollers for example, were found to strongly correlate with the locus of sign changes in the streamwise component of wall shear -at least during the early acceleration phases- as indicated by the thick red lines in Figs. 4, 5, 10 and 11. Their location and evolution can be simply related to incipient sediment motion if one considers the stress distribution they generate. By generating a line of stress divergence along the spanwise direction, they tend to concurrently push sediment towards both the upwind crest and the downstream one. Thus, they generate a scouring effect at the ripple trough which periodically transfers sediment towards both crests. In the presence of a current, they are therefore expected to generate asymmetric crests, because during flow reversal spanwise rollers become more energetic during flow reversal (see Fig. 5).

Lambda structures could be responsible for incipient sediment motion and suspended sediment transport in planes perpendicular to the flow direction, i.e., laterally and vertically. Figure 12 presents the "anatomy" of such a structure with the quadrant events superimposed. Their legs close to the wall are clearly associated with a local

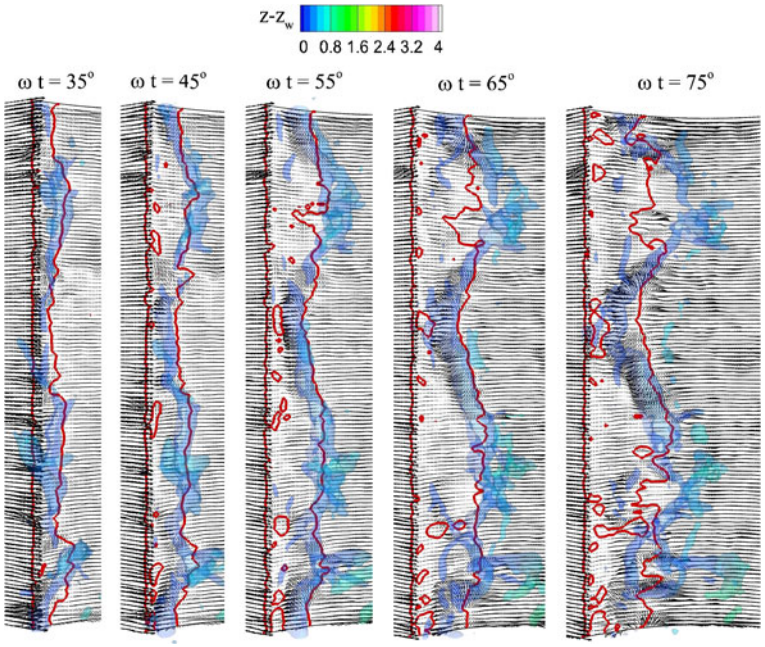

Fig. 11 Evolution of the primary roller during $\omega t = 35 - 75°$ at intervals of 10° for Case A0. The *red line* is the locus of sign change for the streamwise component of wall shear stress and the *color* corresponds to the local distance of the structure from the wall

variation of the shear stress along the bed. At their part in contact with the wall, these lambda structures have their legs rotating in a typical clockwise/counterclockwise fashion. This pattern of rotation, generates lines of stress divergence at their legs and a region of stress convergence between them (top of Fig. 7). Therefore, the existence of lambda structures would be expected to: (i) push transported sediment between the legs of the structure forming a secondary single ripple parallel to the flow and (ii) scour the bed at the legs generating two secondary troughs oriented along the streamwise direction.

The rotational pattern between the legs of lambda structures was also found to generate extremely strong, vertical suction currents from the wall as shown in Fig. 12. The intensity of these currents even for Case B0, was frequently equal to -and in some cases even bigger than- the amplitude U_o of the external flow. These strong instantaneous ejections are clearly illuminated by a large ejection region (Q_2, shown as green region) at the inner part of the structure which was literally ejecting fluid from the wall to the outer flow. The outer shell of the structure was dominated by Q_4 sweep events closer to the wall and interaction events further away from the wall. Thus, the passage of a lambda structure could be also associated with the uplift of sand grains and suspension.

Arch-shaped structures (tornado-like) on the other hand, could result in local scouring as well as redistribution of suspended sediment. As shown in Fig. 13, the part of the arch-shaped structure in contact with the wall generates a line of stress convergence parallel to the outer flow. This stress distribution could set in motion sediment

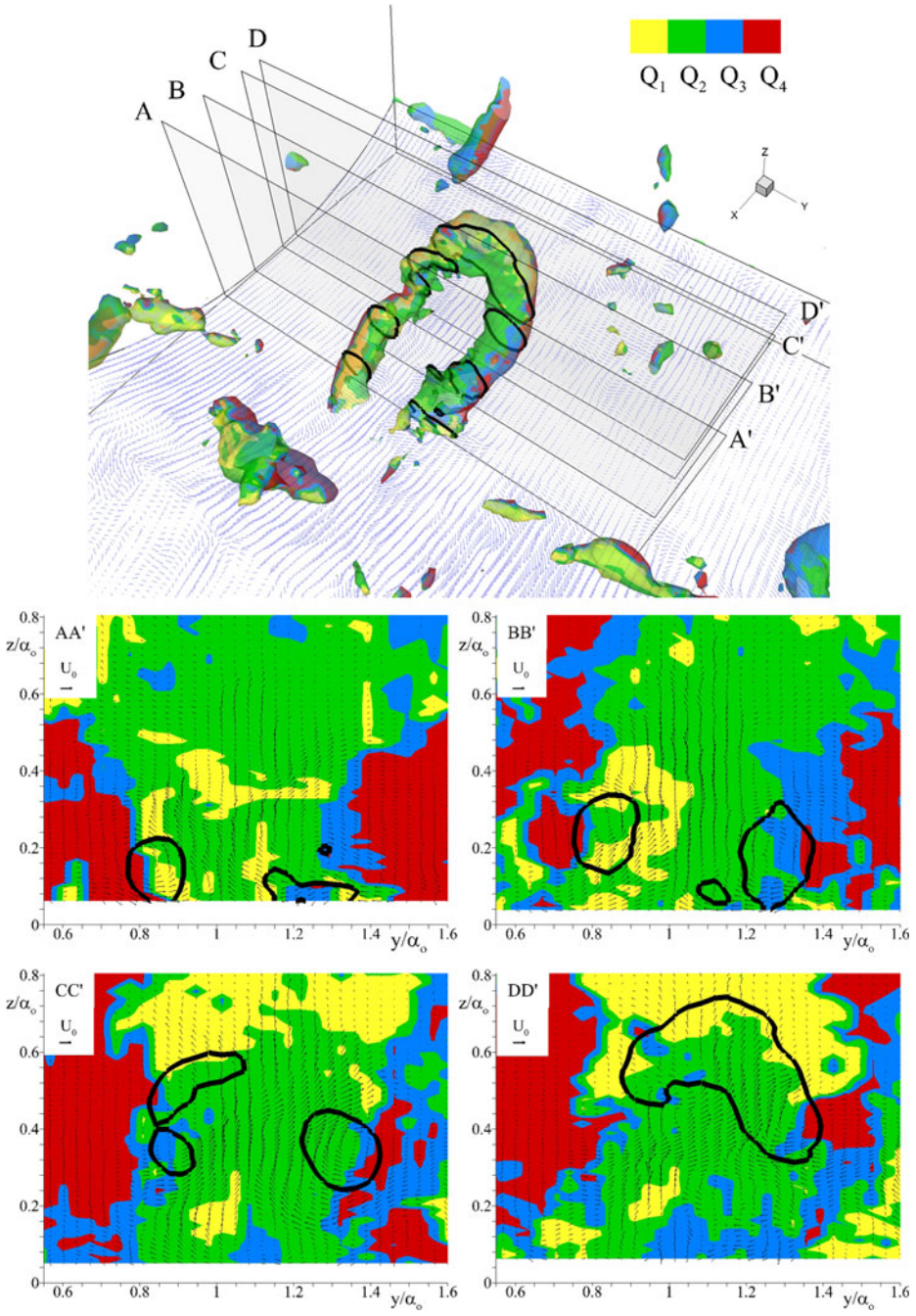

Fig. 12 Snapshot of a lambda coherent structure (*upper figure*) for Cases B0, and its cross-sections (*bottom figures*). The *color* corresponds to the local quadrant event

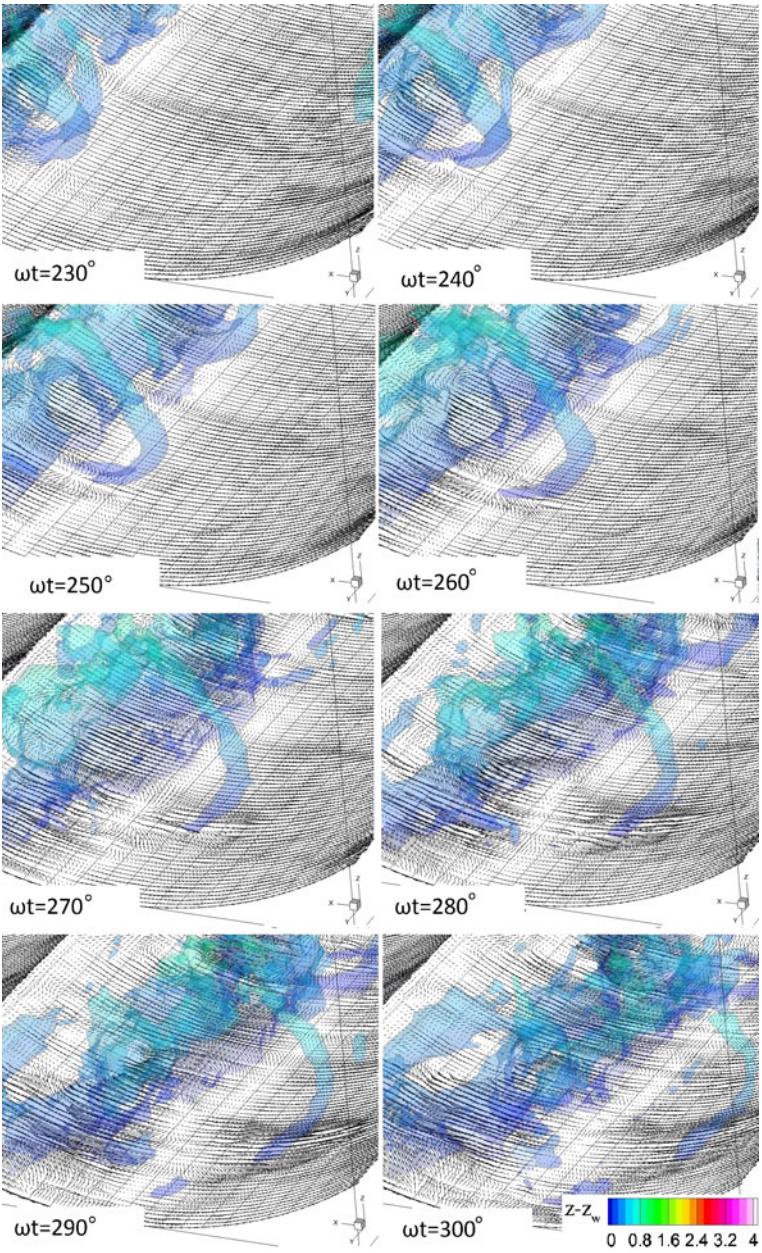

Fig. 13 Evolution of wall shear stress below an arch-like structure for case B0 during $\omega t = 230 - 300°$. The *color* corresponds to the local distance from the wall

from the bed along the spanwise direction as the structure travels downstream. Therefore, the existence of these structures could result in local scouring along their footprint in the streamwise direction (Fig. 13) and the formation of a secondary streamwise trough along an erodible bed. In cases where these structures survive

long enough to collapse along the bed, such an event is expected to take place rapidly following the sudden increase of the local wall shear stress along the line of their collapse. On the other hand, the upper part of these structures away from the wall due to its rotation, could result in the redistribution of suspended sediment in the horizontal directions.

5 Conclusions

Large-eddy simulations of oscillatory turbulent boundary layers over a fixed rippled bed with and without a mean current have been presented. The coherent structures generated and evolving in these flows were identified and examined with respect to their anticipated effects on the shear stress distribution along the bed.

Analysis of the examined cases indicates that three fundamentally different coherent flow structures generate, evolve and interact over the ripples. The effect of ripple steepness on these structures was found to be the most significant, with the higher ripples generating more energetic and larger structures that tend to entrain and penetrate deeper inside the external flow. In all cases, the reversal of pressure gradient seemed to destroy the coherency of structures. The effect of current strength was found to be relatively weaker and was only evident after flow reversal when the oscillation opposed the current, leading to a significant growth of coherent structure size.

Acknowledgements The authors would like to thank Prof. J. Fredsœ and Prof. B.M. Sumer for providing validation data for our simulations and several clarifications on the analysis presented in [11].

References

1. Albayrak, I., Hopfinger, E.J., Lemmin, U.: Near-field flow structure of a confined wall jet on flat and concave rough walls. J. Fluid Mech. **606**, 27–49 (2008)
2. Balaras, E.: Modeling complex boundaries using an external force field on fixed Cartesian grids in large-eddy simulations. Comput. Fluids **33**, 375–404 (2004)
3. Barr, B.C., Sinn, D.N., Pierro, T., Winters, K.B.: Numerical simulation of turbulent, oscillatory flow over sand ripples. J. Geophys. Res. **109**(C09009) (2004). doi:10.1029/2002JC001709
4. Bowles, R.I.: Transition to turbulent flow in aerodynamics. Philos. Trans. R. Soc. Lond. A **358**, 245–260 (2000)
5. Calhoun, R., Street, R.: Vortical structures in flow over topography: an LES at laboratory-scale. In: Proc. 13th Symp. on Boundary Layers and Turbulence, pp. 227–230. AMS, New York (1999)
6. Calhoun, R., Street, R.: Turbulent flow over a wavy surface: neutral case. J. Geophys. Res. **106**, 9277–9294 (2001)
7. Chou, Y.-J., Fringer, O.B.: A model for the simulation of coupled flow-bed form evolution in turbulent flows. J. Geophys. Res. Oceans **115**, C10041 (2010)
8. Chang, Y.S., Scotti A.: Entrainment and suspension of sediments into a turbulent flow over ripples. J. Turbul. **4**(19), 1–22 (2003)
9. Ducros, F.D., Comte, P.C., Lesieur, M.: Large-eddy simulation of transition to turbulence in a boundary layer developing spatially over a flat plate. J. Fluid Mech. **326**, 1–36 (1996)
10. Fredsøe, J., Deigaard, R.: Mechanics of Coastal Sediment Transport. World Scientific, Singapore (1992)
11. Fredsøe, J., Andersen, K.H., Sumer, B.M.: Wave plus current over a ripple-covered bed. Coast. Eng. **38**, 177–221 (1999)
12. Grigoriadis, D.G.E., Balaras, E., Dimas, A.A.: Large-eddy simulation of wave turbulent boundary layer over rippled bed. Coast. Eng. **60**, 174–189 (2012)
13. Grigoriadis, D.G.E., Balaras, E., Dimas, A.A.: Large-eddy simulations of unidirectional water flow over dunes. J. Geophys. Res. **114**(F02022) (2009). doi:10.1029/2008JF001014

14. Henn, D.S., Sykes, R.I.: Large-eddy simulation of flow over wavy surfaces. J. Fluid Mech. **383**, 75–112 (1999)
15. Hino, M., Kashiwayanagi, M., Nakayama, A., Hara, T.: Experiments on the turbulence statistics and the structure of a reciprocating oscillatory flow. J. Fluid Mech. **131**, 363–400 (1983)
16. Hopfinger, E.J., Kurniawan, A., Graf, W.H., Lemmin, U.: Sediment erosion by Görtler vortices: the scour- hole problem. J. Fluid Mech. **520**, 327–334 (2004)
17. Hunt, J.C.R., Wray, A.A., Moin, P.: Eddies, streams and convergence zones in turbulent flows. In: Proceedings of the 1988 Summer Program, p. 193. Center for Turbulence Research (1988)
18. Jensen, B.L, Sumer B.M., Fredsœ, J.: Turbulent oscillatory boundary layers at high Reynolds numbers. J. Fluid Mech. **206**, 265–297 (1989)
19. Jeong, J., Hussain, F.: On the identification of a vortex. J. Fluid Mech. **285**, 69–94 (1995)
20. Maaß, C., Schumann, U.: Direct numerical simulation of separated turbulent flow over a wavy boundary. In: Hirsche, E.H. (ed.) Flow Simulation with High Performance Computers. Notes on Numerical Fluid Mechanics, vol. 52, pp. 227–241 (1996)
21. Nielsen, P.: Dynamics and geometry of wave-generated ripples. J. Geophys. Res. **86**(C7), 6467–6472 (1981)
22. O'Donoghue, T., Doucette, J.S., van der Werf, J.J., Ribberink, J.S.: The dimensions of sand ripples in full-scale oscillatory flows. Coast. Eng. **53**, 997–1012 (2006)
23. Osborne, P.D., Vincent, C.E.: Vertical and horizontal structure in susspended sand concentrations and wave-induced fluxes over bedforms. Mar. Geol. **131**, 195–208 (1996)
24. Ribberink, J.S., van der Werf, J.J., O'Donoghue, T., Hassan, W.N.M.: Sand motion induced by oscillatory flows: Sheet flow and vortex ripples. J. Turbul. **9**(20), 1–32 (2008)
25. Salon, S., Armenio, V., Crise, A.: A numerical investigation of the Stokes boundary layer in the turbulent regime. J. Fluid Mech. **570**, 253–296 (2007)
26. Salon, S., Armenio, V., Crise, A.: A numerical investigation of the turbulent StokesEkman bottom boundary layer. J. Fluid Mech. **684**, 316–352 (2011)
27. Scandura, P., Blondeaux, P., Vittori, G.: Three-dimensional oscillatory flow over steep ripples. J. Fluid Mech. **412**, 355–378 (2000)
28. Scotti, A., Piomelli, U.: Numerical simulation of pulsating turbulent channel. Phys. Fluids **13**(5), 1367–1384 (2001)
29. Wallace, J.M., Eckelmann, H., Brodkey, R.S.: The wall region in turbulent shear flow. J. Fluid Mech. **54**(1), 39–48 (1972)
30. Wiberg, P.L., Harris, C.E.: Ripple geometry in wave-dominated environments. J. Geophys. Res. **99**(C1), 775–789 (1994)
31. Wilcox, D.C.: Turbulence Modeling for CFD, 2nd edn. DCW Ind., La Canada, California (1998)
32. Zedler, E.A., Street, R.L.: Large-eddy simulation of sediment transport: current over ripples. J. Hydraul. Eng. **127**, 444–452 (2001)
33. Zedler, E.A., Street, R.L.: Sediment transport over ripples in oscillatory flow. J. Hydraul. Eng. **132**, 180–193 (2006)